Geophysical Research Letters

RESEARCH LETTER
10.1029/2020GL087854

Effect of Fluid Viscosity on Earthquake Nucleation

C. Cornelio[1] and M. Violay[1]

[1]Laboratory of Experimental Rock Mechanics, IIC, ENAC, EPFL, Station 18, Lausanne, Switzerland

Key Points:
- We performed velocity-step experiments in the presence of fluids with different viscosities
- In the presence of viscous fluid on the slip plane, the state variable of rate-and-state frictional laws represents the state of the fluid
- $(a - b)$ rate-and-state frictional parameters depend on effective normal stress and fluid viscosity

Supporting Information:
- Supporting Information S1

Correspondence to:
C. Cornelio,
chiara.cornelio@epfl.ch

Citation:
Cornelio, C., & Violay, M. (2020). Effect of Fluid Viscosity on Earthquake Nucleation. *Geophysical Research Letters*, *47*, e2020GL087854. https://doi.org/10.1029/2020GL087854

Received 6 MAR 2020
Accepted 11 MAY 2020

Abstract Injection of fluids in geo-reservoirs can reduce the effective stresses at depth, lubricating the nearby faults, promoting slip and, potentially, earthquakes. High-viscous fluids are often used during hydraulic fracturing and production phases in geo-reservoirs. Here, we performed dedicated experiments to study the influence of fluid viscosity on earthquake nucleation. We performed frictional sliding experiments at 30 and 50 effective normal stresses and fluids viscosity ranging from 1 to 1,226 mPa s and modeled them with a rate-and-state friction law. In the presence of fluid, the state variable is defined as the ability of the fluid to flow. Our results showed that static friction slightly decreases with increasing viscosity, the dynamic friction is governed by the dimensionless Sommerfeld number ($S = 6\eta VL/(\sigma'_n H^2)$). Moreover, we observed that the $(a - b)$ parameters of the rate-and-state friction law decrease with increasing viscosity down to $(a - b) < 0$, possibly promoting unstable slip and earthquake nucleation.

Plain Language Summary In the last 30 years, the exponential worldwide increase of human-induced seismicity has become an important issue in solid earth sciences. Most of the induced seismicity is due to engineering operations in deep geo-reservoirs for hydrocarbon production, CO_2 storage, wastewater disposal, and the exploitation of geothermal resources. While the reactivation of faults at the origin of this seismicity has been extensively studied, the influence of fluid properties including its viscosity has been overlooked, even if the viscosity of injected fluids spans from that of water to that of honey. In this study, we discuss the influence of fluid viscosity on the nucleation of earthquakes in fluid-permeated experimental faults and on induced earthquakes. Our experimental observations suggest that the viscosity of the fluid does not influence the fault strength. Instead, the viscosity of the fluid controls the behavior of the fault from stable to unstable sliding.

1. Introduction

In the last 30 years, the increase in human-induced earthquakes associated with wastewater disposal, gas storage, or geothermal exploitation (Ellsworth, 2013; Zoback, 2007) has become an important scientific and social issue. As a consequence, the seismic activity rates increased in stable continental regions far from active tectonic margins (Calais et al., 2016). The principal explanation has been that long-term fluid injections nearby preexisting faults can (a) modify the stress field conditions of the fault by changing the reservoir volume and stresses or can (b) decrease the effective normal stress acting on a fault causing its reactivation (Ellsworth, 2013; Keranen et al., 2013; King Hubbert & Rubey, 1959; McGarr et al., 2015; Weingarten et al., 2015). Under this condition, fluid overpressure is not the only parameter governing fault reactivation and the associated seismicity. The injection procedures (Noël et al., 2019) and the fluid thermal and physical properties (Acosta et al., 2018) are also key parameters to understand fault reactivation. Moreover, in geoengineering practice, the viscosity of the injected fluids varies over four orders in magnitude, from 0.001 Pa s for liquid water to ~0.1 for wastewater disposal (Fu, 2017; Lu & Wei, 2011; Szafranski & Duan, 2018), up to ~10 Pa s for fracturing fluids (Cornelio & Violay, 2020; Esmaeilirad et al., 2016; Esmaeilirad et al., 2016; Gulbis & Hogde, 2000; Zhang et al., 2010).

The fluid injection procedure can involve long-term low-pressure injections to minimize the associated seismicity. In this situation, a viscous fluid might have time to diffuse and flow throughout the whole rupture area of the fault surface.

Furthermore, recent experimental studies have shown that fluid viscosity controls seismic source parameters, including stress drops, the weakening distance, weakening rate, and the earthquake energy budget (Cornelio et al., 2019, 2020).

To model the mechanical behavior of these earthquakes, the failure conditions to initiate rupture are often treated using the isotropic Mohr-Coulomb theory, where the critical shear stress (τ_{crit}) is given by $\tau = \mu$

$(\sigma_n - P_f)$, where τ and σ_n are the shear stress and the normal stress that act on the fault plane, respectively; μ is the coefficient of friction; and P_f is the pore pressure (Beeler & Tullis, 1997). On the other hand, the slip behavior during fault reactivation, that is, the earthquake potential of a fault is often modeled with rate-and-state friction (RSF) laws, which provide a comprehensive analysis of the slip behavior. In this framework, the frictional response of a fault varies with the previous loading history and depends on both the instantaneous slip rate (V) and a state variable (θ) that considers the gradual evolution of the sliding interfaces (Dieterich, 1978; Ruina, 1983). The RSF theory suggests that stable sliding is favored by increasing pore fluid pressure and a low injection rate (Heslot et al., 1994; Ikari et al., 2009; Niemeijer & Collettini, 2014; Noël et al., 2019; Scholz, 1998; Scuderi & Collettini, 2016; Segall & Rice, 1995). However, how the viscosity affects the evolution of the rate-and-state friction parameters and therefore the fault stability itself are currently not clear.

In this work, we conducted frictional sliding experiments in a vertically saw-cut triaxial configuration at different effective normal stresses. We have run tests under dry (room humidity) and low- to high-viscous fluid fault saturated conditions. Further, we examine the stability behavior of the fault under these end-member conditions in the light of the rate-and-state frictional parameters. Here, we attempt to quantify the frictional strength and stability of granitic faults saturated with viscous fluids.

2. Methods

We performed frictional tests using a recently installed triaxial deformation apparatus, oil-confining medium called FIRST (Figure 1a), located at EPFL, Switzerland (supporting information Text S1 and Figure S1). The apparatus can reach 200-MPa confinement pressure, 1.6-GPa axial load, and 200-MPa fluid pressure, on 38-mm diameter samples. The tests were conducted on bare surfaces in an axially precut configuration on Lapeyrate granite cylinders (Figure S2), following the method described in Harbord et al. (2017). The experimental assembly consists of two semicylinders of 37-mm diameter cut along a vertical axis plane (Figure 1b). Before beginning the experiments, the two half cylinders are offset using approximately 10-mm-high silicon spacers, creating an initial contact area of ~1,950 mm^2, allowing up to 5-mm displacement. Sliding surfaces were roughened using 120 SiC abrasive paper to produce an initial roughness of ~3 μm (Figure S3). The normal stress on the fault equals the confining pressure, $\sigma_n = P_c$, and shear stress, τ, is proportional to the pressure of the vertical piston:

$$\tau = \sigma_a \, A_0 / A_{\text{sliding}},$$

where A_0 is the two semicylinder base area and A_{sliding} is the sliding surface contact area $A_{\text{sliding}} = A_i + 2r\,\delta(t)$, where A_i is the initial contact area, $2r$ is the sample diameter, and δ is the slip of the fault. To facilitate fluid saturation of the fault plane, two 5-mm diameter boreholes having inclinations of ~45° with respect to the fault surface were drilled at ~2.5 mm from the edge of the half-cylinder sample through the material on both sides of the fault (Figure S2). We run experiments under room humidity conditions (i.e., dry in the following figures) with a confining pressure P_c of 30 and 50 MPa. We also performed experiments under drained fault conditions, with four different %weight/%weight mixtures of distilled water and glycerol used as fluids: 100% distilled water (water in the following figures), 40% water/60%glycerol (glyc60 in the following figures), 15%water/85%glycerol (glyc85 in the following figures), and 1%water/99%glycerol (the remaining 1% being impurities; glyc99 in the following figures). Viscosity values were measured using a calibrated Ubbelohde capillary viscometer (Cannon Instrument Company) at a temperature of 20°C (Tables S1 and S2). The experiments in the presence of fluids were conducted at constant effective confining pressures ($P_{c,\text{eff}} = P_c - P_f$) of 30 and 50 MPa and at constant $\lambda = P_f/P_c = 0.2$ (i.e., with $P_f = 6$ and 10 MPa, respectively). At target fluid pressure P_f, we allowed the fluid pressure to equilibrate by waiting 30 min and 2 hr for experiments performed with water and with water/glycerol mixtures, respectively.

The apparent friction (μ) was calculated as the ratio between the shear stress (τ) and the effective normal stress ($\sigma'_n = \sigma_n - P_f = P_{c,\text{eff}}$ in our configuration):

$$\mu = \frac{\tau}{\sigma'_n} = \frac{\tau}{\sigma_n - P_f}.$$

Shear strength (τ) was corrected for the increasing contact area with slip. Static friction (μ_{static}) values were obtained at the end of the elastic loading of the fault (Figure 2a).

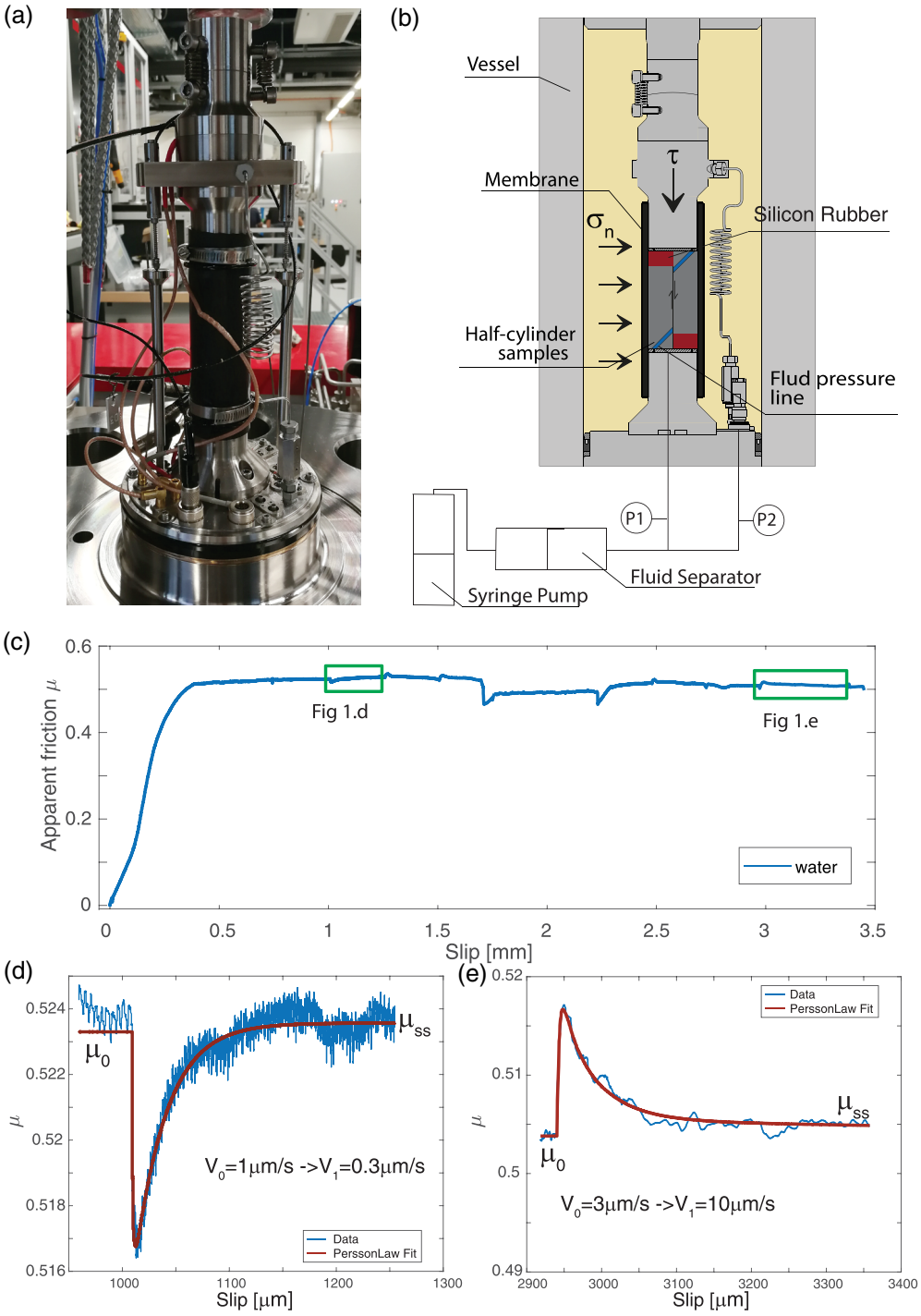

Figure 1. (a) Picture of the sample assembly on the triaxial apparatus FIRST. (b) Sketch of the experimental configuration, fluid pressure lines, and fluid pressure pump. The fluid pressure P_f is the average of the two measured pressures, P1 and P2. A fluid separator is used for the experiments performed in the presence of viscous fluids. (c) Experimental curves of the evolution of the apparent friction $\mu = \tau/\sigma' n$ versus the slip of the fault for experiment ds042 (blue curve) performed under water saturated conditions at 50-MPa effective normal stress. Green rectangles correspond to zoom-in panel (d) and (e). (d) Model inversion of the experimental data with the Persson law resulting in rate-and-state values of a and b for a velocity step from $V_0 = 1$ μm/s to $V_1 = 0.3$ μm/s. (e) Model inversion of the experimental data with the Persson law resulting in rate-and-state values of a and b for a velocity step from $V_0 = 3$ μm/s to $V_1 = 10$ μm/s.

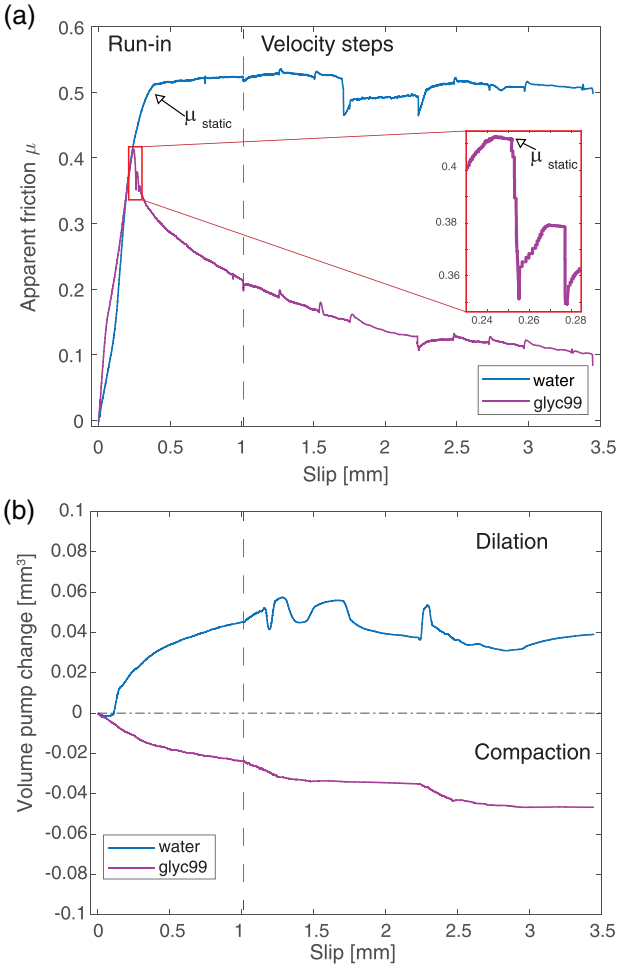

Figure 2. Experimental curves. (a) Experimental curves of the evolution of the apparent friction $\mu = \tau/\sigma' n$ versus the slip of the fault for experiment ds042 (blue curve) performed under water saturated condition at 50-MPa effective normal stress and ds050 (magenta curve) performed under glycerol 99 saturated conditions at 50-MPa effective normal stress. Zoom of the initial stick-slip in the red box. (b) Evolution of the change in fluid volume in centimeters cubed during shearing for experiment ds042 (blue curve) performed under water saturated conditions at 50-MPa effective normal stress and ds050 (magenta curve) performed under glycerol 99 saturated conditions at 50-MPa effective normal stress. Compaction corresponds to a negative fluid volume change; dilation corresponds to a positive fluid volume change.

To get insight into fault stability, we studied the slip-rate dependence of friction by imposing different velocity steps (0.3-1-3-10-0.3-1-3-10 μm/s) for a total displacement of 2.5 mm (Figure S4). The data were recorded at a maximum of 100 Hz. For each step, we suddenly increased the slip rate (i.e., velocity step), inducing an immediate increase in apparent friction followed by an exponential decay over some critical slip distance (d_c) to a new steady-state value of the frictional resistance (Scholz, 1998). To retrieve the rate and state frictional constitutive parameters, we modeled each velocity step with the empirical law for apparent friction evolution as a function of time and slip rate:

$$\mu = \mu_0 + a\ln\left(\frac{V}{V_0}\right) + b\ln\left(\frac{V_0\theta}{d_c}\right),$$

where μ_0 is the value of the apparent friction coefficient during steady-state slip at slip rate V_0, V is the frictional slip rate, θ is a state variable (Ruina, 1983), and a and b are empirical constants. We used the Ruina slip-dependent evolution law for the experiments performed under room-humidity conditions (and in the presence of water for comparison):

$$\dot{\theta} = -\frac{V\theta}{d_c}\ln\left(\frac{V_0\theta}{d_c}\right)$$

Moreover, we used the Persson state evolution law for the experiments performed in the presence of all fluids on the fault. The Persson state evolution law comes from the idea that the transition between stable and unstable behavior of a system permeated with fluid depends on the nucleation of solid structures in a lubricated film (Persson, 2000a, 2000b).

$$\dot{\theta} = (1-\theta)(-\ln(1-\theta))^{\frac{2}{3}} - \frac{\theta V}{d_c},$$

where d_c is a characteristic length over which the solid structures in the lubrication film start to behave as a fluid. The Persson state evolution law can only be used when sliding in the presence of viscous fluid is in the boundary lubrication regime.

In fact, when sliding on a lubricated surface, three regimes of lubrication are possible: boundary lubrication regime (BL), mixed regime (ML), and elastohydrodynamic lubrication (EHD). The transition from one regime to another is governed by the dimensionless Sommerfeld number S, defined as $S = 6\eta VL/(\sigma'_n H^2)$, where η is the fluid viscosity at the mean estimated surface temperature under steady-state conditions, L is the characteristic slip length, and H is the initial average asperity height. For low values of S ($S < 10^{-3}$, i.e., boundary lubrication regime), the normal stress is supported by the solid-solid contacts. For high values of S ($S > 1$, i.e., fully lubricated regime), the normal stress is supported by the interstitial fluid; and for intermediate values of S ($10^{-3} < S < 1$, i.e., mixed lubricated regime), the normal stress is partially supported both by the solid-solid contacts and by the fluid. For each velocity step between slip rate V_0 and V, we computed S at steady state with $H = 3$ μm as the initial asperity height (see Figure S3) and L as equal to the length of the contact area evolving with slip $L = L_i + \delta$, where L_i is the length of the sample minus the length of the silicon spacer. σ'_n is the effective normal pressure.

3. Results

At the beginning of the experiments, during the sample loading phase at 1-μm/s slip rate, the shear stress acting on the fault increased until the static friction coefficient was overcome and slip was initiated.

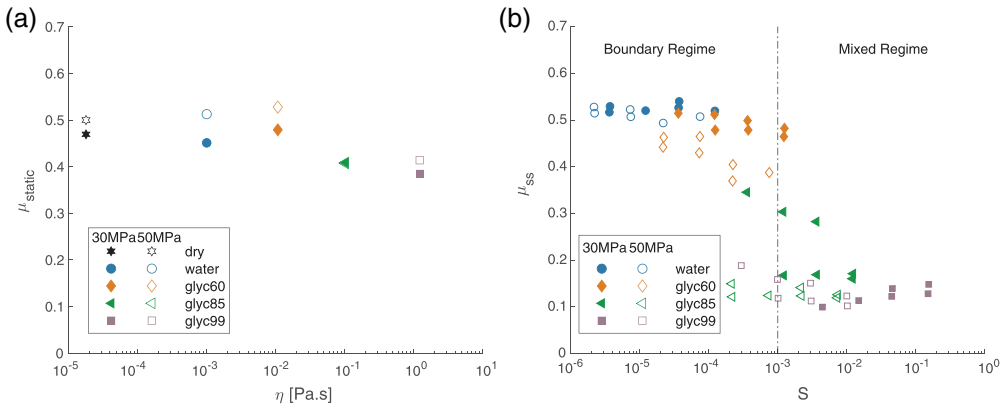

Figure 3. Static and steady state friction coefficients. (a) Static friction coefficient μ_{static} versus viscosity of the fluid on the slipping surface. For the experiments performed under room humidity conditions, the viscosity of the air ($\eta = 1.88 \times 10–5$ Pa s) trapped in the slip zone was used. (b) The steady state friction coefficient for each velocity step versus the computed Sommerfeld number. The Sommerfeld number allows us to distinguish the velocity steps in the boundary lubrication regime and the velocity steps in the mixed regime. Full markers for experiments performed at effective normal stress of 30 MPa, and empty markers for experiments performed at 50-MPa effective normal stress.

Immediately following this, the faults showed different behavior as a function of the fluid trapped on the fault surface (Figures 1c and 2a). During experiments performed under room-humidity conditions and in the presence of water, both at 30- and 50-MPa effective normal stress, slip hardening behavior was observed. Indeed, at 30-MPa effective confining pressure, the apparent friction increased from the static value 0.481 (μ_{static}) to 0.531 under room-humidity condition. In the presence of water, the static friction coefficient increased from 0.451 (μ_{static}) to 0.540. The experiments at 50-MPa effective confining pressure performed under room-humidity conditions and in the presence of water showed a slip neutral behavior with constant apparent friction coefficients where were equal to the static values ($\mu_{static} = 0.499$ for room humidity and $\mu_{static} = 0.513$ for water) (Figure S4).

On the contrary, the experiments performed in the presence of more viscous fluids ($\eta > 10.8$ mPa s, i.e., glyc60, glyc85, and glyc99) showed a slip softening behavior. For example, for glyc85, the apparent friction decays from the static value 0.409 (μ_{static}) to 0.371 at 30 MPa and from 0.408 (μ_{static}) to 0.155 at 50 MPa. For glyc99, the apparent friction decays from the static value 0.385 (μ_{static}) to 0.108 at 30 MPa and from 0.412 (μ_{static}) to 0.213 at 50 MPa.

Regarding the fault stability, independent of the macroscopic behavior of the fault (i.e., slip neutral or slip softening), each velocity step reached a detrended steady state friction coefficient (Figure 3b). We observed a decay of the μ_{ss} with an increase of the Sommerfeld number from values ranging between 0.4 and 0.6 in boundary lubrication regime and between 0.1–0.3 in mixed lubrication regime.

Importantly, the experiments performed at 50 MPa and with fluids characterized by $\eta \geq 10.8$ mPa s showed stick-slip behavior during the initial phase of loading (see Figures 2a and S4). Furthermore, to better understand the effect of viscosity on the stability of the fault and earthquake nucleation, we model the sample's frictional response to velocity steps for the experiments performed in boundary regimes with a rate-and-state law (Carlson & Batista, 1996). The limit between the boundary regime and the mixed lubrication regime was set at $S < 10^{-3}$ following Cornelio et al. (2019) (Figure 2b).

For experiments performed at 30 MPa effective normal stress, $(a - b)$ values are comprised between 0.001 and 0.009, that is, velocity strengthening behavior, for experiments performed under room-humidity condition; between 0.003 and 0.009 for experiments performed under water fault saturated condition; between 0.001 and 0.004 for experiments performed under glyc60 fault saturated condition; and between 0.003 and 0.0049 for experiments performed under glyc85 fault saturated condition (Table S1). For experiments performed at 50 MPa effective normal stress, $(a - b)$ values are comprised between −0.003 and − 0.004, that is, velocity weakening behavior, under room-humidity condition; 0 and 0.006 for experiments performed under water fault saturated condition; −0.001 and 0.004 for experiments performed

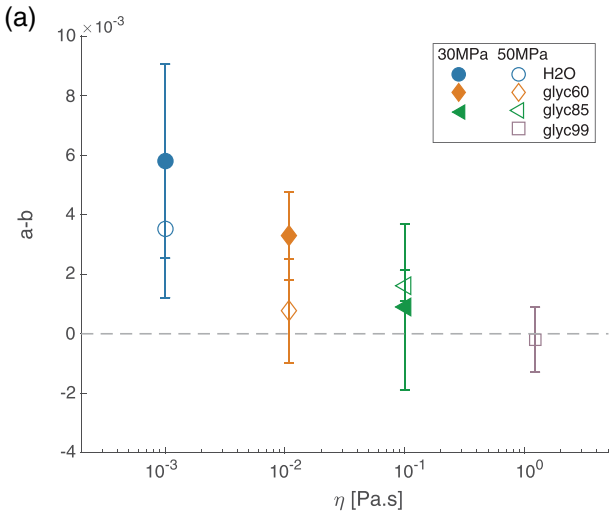

Figure 4. Average values of $(a - b)$ rate and state parameters versus viscosity of the fluid for experiments performed under fault fluid saturated conditions and under boundary lubrication regime. The parameters were obtained using the Persson state law coupled with the friction empirical law. Full markers for experiments performed at 30-MPa effective normal stress, and empty markers for experiments performed at 50-MPa effective normal stress.

under glyc60 fault saturated condition; −0.001 and 0.002 for experiments performed under glyc85 saturated condition; and approximately −0.001 for experiments performed under glyc99 fault saturated condition (Table S2).

The fluid volume evolution during shearing showed two opposite behaviors as a function of the fluid composition. The experiments performed with water suggested general dilatant trends while the experiments performed with mixtures of water and glycerol or pure glycerol showed generally compaction. We estimated the change of the fluid layer thickness (ΔH) using the evolution of the fluid volume change (ΔV) during experiments, under the hypothesis that fluid volume variation happens only on the fault plane (maximum possible value of ΔH):

$$\Delta H = \Delta V / (2r^* L_{\text{tot}}),$$

where $L_{\text{tot}} = L + L_{\text{rubber}}(\delta)$ and $L_{\text{rubber}}(\delta) = L_{\text{rubber},0} - \delta$ are the length of the silicon spacer deforming elastically with slip and defined as the difference between the initial length $L_{\text{rubber},0}$ and the slip (δ). The experiments showed a negligible change of ΔH and, as a consequence, of the initial H. Importantly, no layer of gouge material was recovered on the sample surfaces after experiments performed in the presence of fluids, suggesting that ΔH is not affected by wear processes.

4. Discussion

In agreement with previous studies conducted under room humidity condition, in the presence of water (Passelègue et al., 2016) and in the presence of more viscous fluids (Cornelio et al., 2019), μ_{static} was independent of the effective normal stress and decreased slightly with increasing fluid viscosity (from ~0.50 under room-humidity conditions and at η = 1.001–10.8 mPa s to ~0.39 at η = 1,226 mPa s) (Figure 3a), indicating that the highly viscous fluids only had a marginal effect on the frictional strength of the fault rocks.

On the contrary, the apparent friction coefficient showed a systematic decay with slip (Figures 2a and S4), depending of the fluid viscosity. In particular the friction coefficient at the steady state of each velocity step, μ_{ss}, decreased with an increasing Sommerfeld number S (Figure 3b). This behavior can be described by an elasto-hydrodynamic theory as detailed in Cornelio et al. (2019). However, note that here the data are highly scattered, because μ_{ss} is controlled by both the effect of the lubrication of the fault by the presence of fluid and by the performed velocity steps.

Under the boundary lubrication regime, the direct effect parameter (a) of the rate-and-state law was independent of the fluid viscosity (Figure S6a), the evolutive effect parameter (b) increased with viscosity (Figure S6b), and the critical distance d_c showed no clear tendency with viscosity (Figure S6c). Therefore, the $(a - b)$ values of the rate-and-state law decreased for larger values of viscosity (Figure S7). In particular, for the highest viscosity (η = 1,226 mPa s), we observed a transition to negative values of $(a - b)$ (Figure 4). Negative values suggest unstable slip behavior and potential earthquake nucleation. We point out that the fluid water experiments were modeled with both the slip evolution dependent law (Ruina, 1983) and the Persson state evolution law (Persson, 2000b) and showed only small differences (~10− 4) (Table S3 and Figure S5). Furthermore, the increase of the fluid viscosity can reduce the hydraulic diffusivity of the fault following ($\alpha_{\text{hy}} = k/(\beta\eta)$), where k is the permeability of the material and β is the storage capacity. For example, Faulkner et al. (2018) observed a decrease of the $(a - b)$ parameter with a decrease of the hydraulic diffusivity of a layer of gauge, changing the permeability (k) of the gouge layer sandwiched on the fault planes.

Moreover, in agreement with theoretical models (Chambon & Rudnicki, 2001; Dieterich, 1992; He et al., 1998) and previous experimental studies on both bare surfaces (Harbord et al., 2017; Linker & Dieterich, 1992) and gouge materials (Leeman et al., 2018; Marone et al., 1990; Rathbun et al., 2008; Scuderi et al., 2016), and independent of the fluid condition, the increase of the effective normal stress

acting on the experimental fault promoted a decrease of $(a - b)$ values down to negative $(a - b)$ values at 50 MPa (Figure S8). For both gouge materials and sliding on bare surfaces this behavior has been attributed to an increase of the critical stiffness (K_c) of the fault plane. Indeed, combined with the elastic dislocation theory, the rate-and-state formulation states that if the stiffness of the elastic medium (K) is smaller than the critical fault stiffness (K_c), frictional instability can occur. The parameter K_c is defined by the effective normal stress and the rate-and-state constitutive parameters (a, b, and d_c) of the fault: $K_c = ((b - a)(\sigma_n - P_f))/d_c$, where d_c is the critical slip distance and $(b - a)$ is the friction rate parameter.

Finally, the evolution of fluid volumes during shearing suggested a predominant shear-enhanced dilatancy for experiments performed with water. This result is in agreement with the results of Beeler and Tullis (1997) and can be explained as the vertical movement of the fault plane necessary to overcome the asperities. However, when a mixture of water and glycerol or pure glycerol was trapped on the slip surface, the experiment showed only a general compaction behavior. Shear enhanced compaction is due to fluid layer thinning during sliding, which is very efficient at high viscosity.

5. Conclusions and Implications for Induced Seismicity

We conducted 10 vertically saw-cut triaxial experiments on Lapeyrate semi-cylindrical samples with four various fluid viscosities and two effective normal stress. We subjected the fault to variations of the slip-rate in order to estimate the rate and state parameters of the studied system and understand if slip behavior is governed by fluid viscosity. We analyzed our results on the light of the Persson state variable law. The results showed that

1. the fluid viscosity did not influence the static friction coefficient of the faults;
2. steady state friction coefficient decreases with increasing Sommerfeld number in agreement with elasto-hydrodynamic theory;
3. during velocity steps and under the boundary lubrication regime:

a. the increase of normal stress tends to destabilize the fault and
b. the increase of the viscosity of the pressurized fluid on the slip surface tends to destabilize the fault; and
c. high fluid viscosity promotes shear-enhanced compaction.

It is important to recall that high fluid viscosity strongly limits fracture leak off (enhancing the efficiency of the hydro-fracturing mechanism) and reduces diffusion rate in the fault zone, reducing the area over-pressurized by fluids. The area over-pressurized by fluid has an important influence on the probability of earthquake occurrence as observed by Shapiro and Dinske (2009). Our experimental results demonstrated that fluid viscosity has a role in the determination of the empirical $(a - b)$ parameter of an experimental fault. We suggest that a similar behavior can be expected in case of induced seismicity in geo-reservoirs. Under specific conditions of fault geometry and surrounding stress of the fault, high fluid viscosity might favor unstable slip and earthquake nucleation if the system and the reservoir are saturated with viscous fluid.

Data Availability Statement

Correspondence and request for additional material should be addressed to chiara.cornelio@epfl.ch. All the experimental raw data are available in Zenodo with the identifier (https://doi.org/10.5281/zenodo.3698128).

Acknowledgments

This research is funded by the European Research Council Starting Grant project 757290-BEFINE. The authors acknowledge Carolina Giorgetti, Henri Leclère, Francois Passelègue, Federica Paglialunga, and Corentin Noel for scientific discussion and laboratory support. The authors acknowledge Professor C. Ancey and B. de Graffenried for their help with fluid viscosity measurements and scientific discussion and Barnaby Fryer for proofreading.

References

Acosta, M., Passelègue, F. X., Schubnel, A., & Violay, M. (2018). Dynamic weakening during earthquakes controlled by fluid thermodynamics. *Nature Communications*, *9*(1), 3074. https://doi.org/10.1038/s41467-018-05603-9

Beeler, N. M., & Tullis, T. E. (1997). The roles of time and displacement in velocity-dependent volumetric strain of fault zones. *Journal of Geophysical Research*, *102*(B10), 22,595–22,609. https://doi.org/10.1029/97jb01828

Calais, E., Camelbeeck, T., Stein, S., Liu, M., & Craig, T. J. (2016). A new paradigm for large earthquakes in stable continental plate interiors. *Geophysical Research Letters*, *43*, 10,621–10,637. https://doi.org/10.1002/2016GL070815

Carlson, J. M., & Batista, A. A. (1996). Constitutive relation for the friction between lubricated surfaces. *Physical Review E*, *53*(4), 4153–4165. https://doi.org/10.1103/PhysRevE.53.4153

Chambon, G., & Rudnicki, J. W. (2001). Effects of normal stress variations on frictional stability of a fluid-infiltrated fault. *Journal of Geophysical Research*, *106*(B6), 11,353–11,372. https://doi.org/10.1029/2001JB900002

Cornelio, C., Passelègue, F. X., Spagnuolo, E., Di Toro, G., & Violay, M. (2020). Effect of Fluid Viscosity on Fault Reactivation and Coseismic Weakening. *Journal of Geophysical Research: Solid Earth*, *125*(1). https://doi.org/10.1029/2019JB018883

Cornelio, C., Spagnuolo, E., Di Toro, G., Nielsen, S., & Violay, M. (2019). Mechanical behaviour of fluid-lubricated faults. *Nature Communications*, *10*(1), 1274. https://doi.org/10.1038/s41467-019-09293-9

Cornelio, C., & Violay, M. (2020). Parametric analysis of the elastohydrodynamic lubrication efficiency on induced seismicity. *Geophysical Journal International.*, *222*(1), 517–525. https://doi.org/10.1093/gji/ggaa180

Dieterich, J. H. (1978). Time-dependent friction and the mechanics of stick-slip. *Pure and Applied Geophysics PAGEOPH*, *116*(4–5), 790–806. https://doi.org/10.1007/BF00876539

Dieterich, J. H. (1992). Earthquake nucleation on faults with rate-and state-dependent strength. *Tectonophysics*, *211*(1–4), 115–134. https://doi.org/10.1016/0040-1951(92)90055-B

Ellsworth, W. L. (2013). Injection-induced earthquakes. *Science*, *341*(6142), 1,225,942–1,225,942. https://doi.org/10.1126/science.1225942

Esmaeilirad, N., Terry, C., Kennedy, P., & A., & Carlson, K. (2016). Recycling fracturing flowback water for use in hydraulic fracturing: Influence of organic matter on stability of carboxyl-methyl-cellulose-based fracturing fluids. *SPE Journal*, *21*(04), 1358–1369. https://doi.org/10.2118/179723-PA

Esmaeilirad, N., White, S., Terry, C., Prior, A., & Carlson, K. (2016). Influence of inorganic ions in recycled produced water on gel-based hydraulic fracturing fluid viscosity. *Journal of Petroleum Science and Engineering*, *139*, 104–111. https://doi.org/10.1016/j.petrol.2015.12.021

Faulkner, D. R., Sanchez-Roa, C., Boulton, C., & den Hartog, S. A. M. (2018). Pore fluid pressure development in compacting fault gouge in theory, experiments, and nature. *Journal of Geophysical Research: Solid Earth*, *123*, 226–241. https://doi.org/10.1002/2017JB015130

Fu, H. (2017). Treatment of oilfield fracturing wastewater. *Petroleum Science and Technology*, *35*(17), 1743–1749. https://doi.org/10.1080/10916466.2017.1363777

Gulbis, J., & Hogde, R. M. (2000). Chapter 7 Fracturing Fluid Chemistry and Proppant. In M. J. Economides & K. G. Nolte (Eds.), *Reservoir Stimulation* (pp. 7-1–7-23). New York: John Wiley and Sons.

Harbord, C. W. A., Nielsen, S. B., De Paola, N., & Holdsworth, R. E. (2017). Earthquake nucleation on rough faults. *Geology*, *45*(10), 931–934. https://doi.org/10.1130/G39181.1

He, C., Ma, S., & Huang, J. (1998). Transition between stable sliding and stick-slip due to variation in slip rate under variable normal stress condition. *Geophysical Research Letters*, *25*(17), 3235–3238. https://doi.org/10.1029/98GL02518

Heslot, F., Baumberger, T., Perrin, B., Caroli, B., & Caroli, C. (1994). Creep, stick-slip, and dry-friction dynamics: Experiments and a heuristic model. *Physical Review E*, *49*(6), 4973–4988. https://doi.org/10.1103/PhysRevE.49.4973

Ikari, M. J., Saffer, D. M., & Marone, C. (2009). Frictional and hydrologic properties of clay-rich fault gouge. *Journal of Geophysical Research*, *114*, B05409. https://doi.org/10.1029/2008JB006089

Keranen, K. M., Savage, H. M., Abers, G. A., & Cochran, E. S. (2013). Potentially induced earthquakes in Oklahoma, USA: Links between wastewater injection and the 2011 M_w 5.7 earthquake sequence. *Geology*, *41*(6), 699–702. https://doi.org/10.1130/G34045.1

King Hubbert, M., & Rubey, W. W. (1959). Role of fluid pressure in mechanics of overthrust faulting. *Bulletin of the Geological Society of America*, *70*(2), 115–166. https://doi.org/10.1130/0016-7606(1959)70[115:ROFPIM]2.0.CO;2

Leeman, J. R., Marone, C., & Saffer, D. M. (2018). Frictional mechanics of slow earthquakes. *Journal of Geophysical Research: Solid Earth*, *123*, 7931–7949. https://doi.org/10.1029/2018JB015768

Linker, M. F., & Dieterich, J. H. (1992). Effects of variable normal stress on rock friction: Observations and constitutive equations. *Journal of Geophysical Research*, *97*(B4), 4923–4940. https://doi.org/10.1029/92jb00017

Lu, M., & Wei, X. (2011). Treatment of oilfield wastewater containing polymer by the batch activated sludge reactor combined with a zerovalent iron/EDTA/air system. *Bioresource Technology*, *102*(3), 2555–2562. https://doi.org/10.1016/j.biortech.2010.11.103

Marone, C., Raleigh, C. B., & Scholz, C. H. (1990). Frictional behavior and constitutive modeling of simulated fault gouge. *Journal of Geophysical Research*, *95*(B5), 7007–7025. https://doi.org/10.1029/JB095iB05p07007

McGarr, A., Bekins, B., Burkardt, N., Dewey, J., Earle, P., Ellsworth, W., et al. (2015). Coping with earthquakes induced by fluid injection. *Science*, *347*(6224), 830–831. https://doi.org/10.1126/science.aaa0494

Niemeijer, A. R., & Collettini, C. (2014). Frictional properties of a low-angle normal fault under in situ conditions: Thermally-activated velocity weakening. *Pure and Applied Geophysics*, *171*(10), 2641–2664. https://doi.org/10.1007/s00024-013-0759-6

Noël, C., Passelègue, F. X., Giorgetti, C., & Violay, M. (2019). Fault reactivation during fluid pressure oscillations: Transition from stable to unstable slip. *Journal of Geophisical Research: Solid Earth*, *124*, 10,940–10,953. https://doi.org/10.1029/2019JB018517

Passelègue, F. X., Spagnuolo, E., Violay, M., Nielsen, S., Di Toro, G., & Schubnel, A. (2016). Frictional evolution, acoustic emissions activity, and off-fault damage in simulated faults sheared at seismic slip rates. *Journal of Geophysical Research: Solid Earth*, *121*, 7490–7513. https://doi.org/10.1002/2016JB012988

Persson, B. N. J. (2000a). Chapter 9 Boundary lubrication. In *Sliding friction: Physical principles and applications* (pp. 313–334). Berlin, Heidelberg: Springer Berlin Heidelberg. https://doi.org/10.1007/978-3-662-04283-0_9

Persson, B. N. J. (2000b). Chapter 12 Lubricated friction dynamics. In *Sliding friction: Physical principles and applications* (pp. 395–413). Berlin, Heidelberg: Springer Berlin Heidelberg. https://doi.org/10.1007/978-3-662-04283-0_12

Rathbun, A. P., Marone, C., Alley, R. B., & Anandakrishnan, S. (2008). Laboratory study of the frictional rheology of sheared till. *Journal of Geophysical Research*, *113*, F02020. https://doi.org/10.1029/2007JF000815

Ruina, A. (1983). Slip instability and state variable friction laws. *Journal of Geophysical Research*, *88*(B12), 10,359–10,370. https://doi.org/10.1029/JB088iB12p10359

Scholz, C. H. (1998). Earthquakes and friction laws. *Nature*, *391*(6662), 37–42. https://doi.org/10.1038/34097

Scuderi, M. M., Marone, C., Tinti, E., Di Stefano, G., & Collettini, C. (2016). Precursory changes in seismic velocity for the spectrum of earthquake failure modes. *Nature Geoscience*, *9*(9), 695–700. https://doi.org/10.1038/ngeo2775

Scuderi, M. M., & Collettini, C. (2016). The role of fluid pressure in induced vs. triggered seismicity: Insights from rock deformation experiments on carbonates. *Scientific Reports*, *6*(1), 24852. https://doi.org/10.1038/srep24852

Segall, P., & Rice, J. R. (1995). Dilatancy, compaction, and slip instability model hydraulic diffusivity. *Journal of Geophysical Research*, *100*(B11), 22,155–22,171. https://doi.org/10.1029/95JB02403

Shapiro, S. A., & Dinske, C. (2009). Fluid-induced seismicity: Pressure diffusion and hydraulic fracturing. *Geophysical Prospecting*, *57*(2), 301–310. https://doi.org/10.1111/j.1365-2478.2008.00770.x

Szafranski, D., & Duan, B. (2018). Integrating poroelastic effects of wastewater injection and rupture dynamics to understand induced seismicity. *SPE/AAPG/SEG Unconventional Resources Technology Conference 2018,URTC*, *2018*(2014), 1–20. https://doi.org/10.15530/urtec-2018-2902051

Weingarten, M., Ge, S., Godt, J. W., Bekins, B. A., & Rubinstein, J. L. (2015). High-rate injection is associated with the increase in U.S. mid-continent seismicity. *Science*, *348*(6241), 1336–1340. https://doi.org/10.1126/science.aab1345

Zhang, G. M., Liu, H., Zhang, J., Wu, H. A., & Wang, X. X. (2010). Three-dimensional finite element simulation and parametric study for horizontal well hydraulic fracture. *Journal of Petroleum Science and Engineering*, *72*(3–4), 310–317. https://doi.org/10.1016/j.petrol.2010.03.032

Zoback, M. D. (2007). *Reservoir geomechanics*. Cambridge: Cambridge University Press. https://doi.org/10.1017/CBO9780511586477